Revealing the Sequence-Structure-Electronic Property Relation of Self-Assembling π-Conjugated Oligopeptides by Molecular and Quantum Mechanical Modeling

Bryce A. Thurston,[†,‡] Ethan P. Shapera,[¶,‡] John D. Tovar,[*,§,‖,⊥] André Schleife,[*,#,@,△] and Andrew L. Ferguson[*,∇]

†*Center for Integrated Nanotechnologies, Sandia National Laboratories, P.O. Box 5800, Albuquerque, NM 87185 USA*

‡*These authors contributed equally to this work.*

¶*Department of Physics, 1110 W Green St, University of Illinois at Urbana-Champaign, Urbana, IL 61801, USA*

§*Department of Chemistry, Krieger School of Arts and Sciences, Johns Hopkins University, 3400 N. Charles St., Baltimore, MD 21218, USA*

‖*Institute for NanoBioTechnology, Johns Hopkins University, 3400 N. Charles St., Baltimore, MD 21218, USA*

⊥*Department of Materials Science and Engineering, Whiting School of Engineering, Johns Hopkins University, 3400 N. Charles St., Baltimore, MD 21218, USA*

#*Department of Materials Science and Engineering, 1304 W Green St, University of Illinois at Urbana-Champaign, Urbana, IL 61801, USA*

@*Materials Research Laboratory, 104 South Goodwin Avenue, University of Illinois at Urbana-Champaign, Urbana, IL 61801, USA*

△*National Center for Supercomputing Applications, 1205 W Clark St, University of Illinois at Urbana-Champaign, Urbana, IL 61801, USA*

∇*Pritzker School of Molecular Engineering, 5640 South Ellis Avenue, University of Chicago, Chicago, IL 60637, USA*

E-mail: tovar@jhu.edu; schleife@illinois.edu; andrewferguson@uchicago.edu

Abstract

Self-assembled nanoaggregates of π-conjugated synthetic peptides present a biocompatible and highly tunable alternative to silicon-based optical and electronic materials. Understanding the relationship between structural morphology and electronic properties of these assemblies is critical for understanding and controlling their mechanical, optical, and electronic response. In this work, we combine all-atom classical molecular simulations with quantum-mechanical electronic structure calculations to ascertain the sequence-structure-electronic property relationship within a family of Asp-X-X-quaterthiophene-X-X-Asp (DXX-OT4-XXD) oligopeptides in which X is one of the five amino acids {Ala, Phe, Gly, Ile, Val} ({A, F, G, I, V}). Molecular dynamics simulations reveal that smaller amino acid substituents (A, G) favor linear stacking within a peptide dimer whereas larger groups (F, I, V) induce larger twist angles between the peptides. Density functional theory calculations on the dimer show the absorption spectrum to be dominated by transitions between carbon and sulphur p orbitals. Although the absorption spectrum is largely insensitive to the relative twist angle, the highest occupied molecular orbital (HOMO) strongly localizes onto one molecule within the dimer at large twist angles impeding the efficiency of transport between molecules. Our results provide fundamental understanding of the relation between peptide orientation and electronic structure, and offer design precepts for rational engineering of these systems.

Introduction

The spontaneous or directed assembly of peptides into ordered nanoaggregates offers a means for the fabrication of macromolecular materials with desirable structural, functional, and biological properties.[1–5] Synthetic oligopeptides, functionalized to contain π-conjugated subunits, can endow the assembled aggregates with optoelectronic and photophysical properties such as exciton coupling or electron transport.[6–10] In contrast to conventional silicon-based materials, these peptidic systems are of interest in the synthesis of water-soluble and biocompatible nanoaggregates with tunable biological, optical, and electronic properties[11–17] and applications as novel light-emitting diodes, field-effect transistors, and solar cells.[13,18–26]

Deterministic control of structure and function of these peptides through sequence is of great interest as a powerful route for creating designer materials with engineered properties.[27] A large body of experimental and computational work has demonstrated that the structure of self-assembled aggregates of synthetic π-conjugated oligopeptides and their attendant photophysical and electronic properties can be modulated by the peptide sequence and π-conjugated core chemistry.[12,15–17,28–35] However, the fundamental sequence-structure-property relationships linking peptide sequence, structure of the self-assembled aggregates, and the emergent photophysical properties are not yet understood. A body of collaborative experimental and computational[12,29,31,36] studies of oligopeptides in aqueous environments have demonstrated that the chemistry of the amino acid residues proximate to the π-conjugated core can strongly influence the stacking between neighboring oligomers in self-assembled nanoaggregates, and impact the resulting morphological, chiral, mechanical, electronic, and optical properties. Classical mechanical molecular modeling indicates the root of this effect to be differences in the degree to which neighboring oligopeptides align in β-sheet-like motifs.[12,29,36] We are engaged in an ongoing computational and experimental study of a particular class of peptide-π-peptide symmetric triblock synthetic oligopeptides. These possess a polymeric π-conjugated core and peptide wings and allow us to gain a deeper understanding of the factors governing peptide assembly with the goal of designing

novel materials with specifically controlled properties.[12,15–17,28–32,34,37]

A recent experimental study of one such peptide-π-peptide family – the Asp-X-X-quaterthiophene-X-X-Asp (DXX-OT4-XXD) oligopeptides in which X is one of the five amino acids {Ala, Phe, Gly, Ile, Val} ({A, F, G, I, V}) (Fig. 1) – revealed a particularly striking relationship between amino acid composition and excited-state properties of the self-assembled aggregates.[29] The two peptide wings both possess N-to-C directionality progressing away from the OT4 core such that the oligopeptide possesses two C-termini and the terminal Asp residues serve as a molecular trigger for assembly.[38] At high pH (pH>5), the Asp residues are fully deprotonated and large-scale assembly is disfavored due to electrostatic repulsion between oligomers carrying a formal charge of $(-4)e$. At low pH (pH<1), the Asp residues protonate, the oligopeptides become electrically neutral, and large-scale aggregation proceeds driven by hydrophobic effects, hydrogen bonding, van der Waals interactions, and $\pi-\pi$ stacking.[39] The particular X residues were selected for their large differences in steric volume and were shown to result in large differences in the dimensions of the self-assembled aggregates, rheological properties of the resultant gels, electrical conductivity of their dropcast films, and photophysical measurements of their absorption, emission, and circular dichroism spectra.

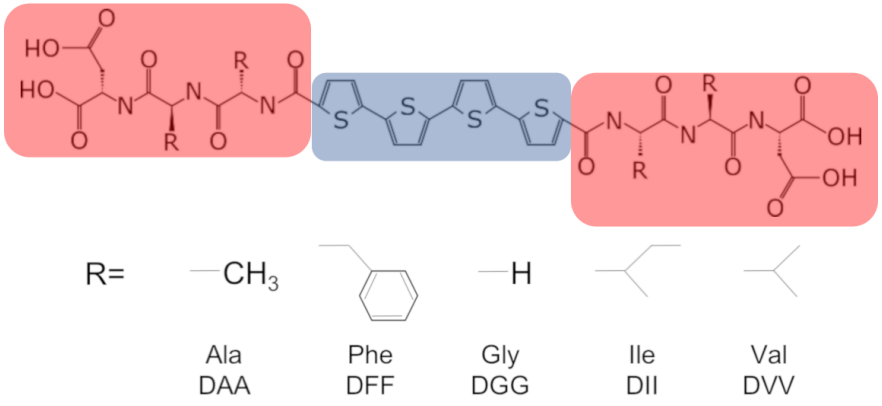

Figure 1: Chemical structure of an Asp-X-X-OT4-X-X-Asp (DXX-OT4-XXD) oligopeptide. The peptide wings (red boxes) flanking the π-conjugated core (blue box) are mirror-symmetric so that the N-to-C directionality progresses away from the core and the oligopeptide possesses two C-termini. The X residues are one of the five amino acids {Ale, Phe, Gly, Ile, Val} with the R groups in the image corresponding to the appropriate side chain.

Whereas the morphological and mechanical properties can be understood in terms of the molecular structure of the nanoaggregates, the electronic and optical properties require an understanding of the influence of oligopeptide stacking upon the overlap and interaction of the π-core orbitals. In particular, the experimental absorption spectra showed marked differences in the measured peak excitation wavelength of the self-assembled nanoaggregates relative to the unassembled monomers as a function of the choice of residue X.[29] The shifts for DGG and DAA were the most pronounced, leading to a blue-shift upon aggregation of $\sim$50 nm as compared with $\sim$10 nm for DFF, DII, and DVV. The origin of this effect is driven by the relative orientations of the π-conjugated cores induced by the peptide wings, but the electronic mechanisms governing this response and its dependence on the geometric configuration of the oligopeptides in the self-assembled nanoaggregates remains unknown.

A number of prior theoretical and experimental studies have been conducted to link the structural and electronic properties in thiophene dimers, crystals, and supramolecular aggregates.[26,40–51] Specifically, these works have quantified interaction energies for various oligothiophene aggregate configurations,[40–43] excited-state properties of oligothiophene monomers and crystals,[46,47,49] and intermolecular charge transfer rates between stacked thiophene cores.[43,48] The modification of packing structure in thiophenes by various linkers has also been studied with density functional theory (DFT) and quantum mechanics / molecular mechanics (QM/MM) approaches.[43,52] However, to the best of our knowledge, the absorption spectra, electronic energy levels, oscillator strengths, density of states, and highest occupied molecular orbital (HOMO) / lowest unoccupied molecular orbital (LUMO) of quaterthiophene aggregates formed in peptide-π-peptide self-assembly have not been previously reported.

In this work we combine classical mechanical molecular modeling with quantum-mechanical electronic-structure calculations to establish fundamental understanding of the sequence-structure-property relationship in the optical response of self-assembled DXX-OT4-XXD peptides. We perform classical molecular dynamics (MD) simulations of the self-assembled

nanoaggregates, followed by DFT calculations on DXX-OT4-XXD dimers over a range of dimer configurations observed in the MD calculations. We resolve the influence of oligopeptide orientation upon the absorption spectra, electronic energy levels, oscillator strengths, density of states, and HOMO/LUMOs to provide new fundamental understanding of the relation between sequence, nanoaggregate morphology, and photophysical absorption in the self-assembly of synthetic peptide-π-peptide oligomers.

Experimental

Molecular dynamics simulations

We performed classical molecular dynamics (MD) simulations for the five peptides DAA, DFF, DGG, DII, and DVV in the DXX-OT4-XXD family (Fig. 1) to obtain representative structures of the self-assembled nanoaggregates. Simulations were conducted using the Gromacs 4.6.7 simulation suite.[53,54] The oligopeptides were modeled using the AMBER99sb force field.[55,56] The Asp residues in each peptide are fully protonated in order to simulate a low pH environment in which large-scale self-assembly of nanoaggregates proceeds.[38] We obtained partial charges for OT4 residues using the restrained electrostatic potential method[57,58] implemented in the RESP/ESP charge Derive Server (REDS)[59] that employs the Gaussian code to perform Hartree-Fock calculations.[60] We note that these Hartree-Fock calculations were used only to estimate a small number of missing partial charges on the OT4 residues required by the AMBER99sb force field to perform the classical MD simulations. The electronic structure calculations on oligopeptide dimers are performed using a completely independent DFT protocol that is described below. Non-bonded parameters were obtained by analogy using the parmchk2 program from Antechamber[61] and the generalized Amber force field (GAFF).[62]

To construct the 1D self-assembled nanoaggregates previously observed in both experiment and simulation,[7,12,29–32,36,38,39,63] we followed the protocol in Ref.[12] to arrange 20

oligopeptide monomers in elongated configurations into a linear stack where each peptide is separated by a center-of-mass distance of $d = 0.45$ nm. Each peptide i in the linear stack is assigned a consistently oriented vector $\mathbf{v}_i$ between the terminal C atoms of the π-conjugated cores. To eliminate steric clashes between nearest neighbors, we commence at one end of the stack and rotate each oligopeptide by a right-handed twist angle of $\theta = 9^\circ$ relative to its immediately preceding neighbor. Twist angles between molecules i and $(i+1)$ are formally defined as $\theta_{i,(i+1)} = \cos^{-1}(\hat{\mathbf{v}}_i \cdot \hat{\mathbf{v}}_{(i+1)}) \cdot sgn((\hat{\mathbf{v}}_i \times \hat{\mathbf{v}}_{(i+1)}) \cdot \hat{\mathbf{d}})$ where $\hat{\mathbf{v}}_i$ is the unit vector oriented along the backbone of molecule i and $\mathbf{d}$ is the unit vector directed from the center of mass of molecule i to molecule $(i+1)$. A schematic of an OT4 dimer illustrating d and θ is presented in Fig. 2. The twisted stacks were then solvated in a rhombic dodecahedral box with TIP3P water molecules,[64] where the box size was fixed to ensure that all peptides are at least 1.0 nm from the edges. Electrostatic interactions were treated using Particle Mesh Ewald (PME) with a cutoff of 1.0 nm and a 0.12 nm Fourier grid spacing that were optimized during runtime.[65] Lennard-Jones interactions were shifted smoothly to zero at 1.0 nm. We fixed bond lengths using the LINCS algorithm,[66] and use Lorentz-Berthelot combining rules to estimate interaction parameters between unlike atoms.[67] Equations of motion were integrated using a leap frog algorithm with a time step of 2 fs.[68]

First, the energy of the system was minimized using the steepest descent algorithm until the maximum force on any atom was less than 1000 kJ/mol·nm. Initial atomic velocities were then assigned by sampling a Maxwell distribution corresponding to 298 K. The system was then subjected to 100 ps of NVT simulation to equilibrate the peptide side chains while the cores were restrained. Temperature was maintained at 298 K using a stochastic velocity rescaling thermostat[69] and a time constant of 0.5 ps. This was followed by 100 ps of NPT simulation employing Berendsen pressure coupling[70] to maintain a pressure of 1.0 atm with a compressibility of 4.6×10^{-5} bar^{-1} and a time constant of 2.0 ps,[71] with the core restraints still in place. Finally, we released the core restraints and conducted 150 ns long NPT simulations to relax the oligopeptide stacks into their equilibrium configurations. During these, a Nosé-

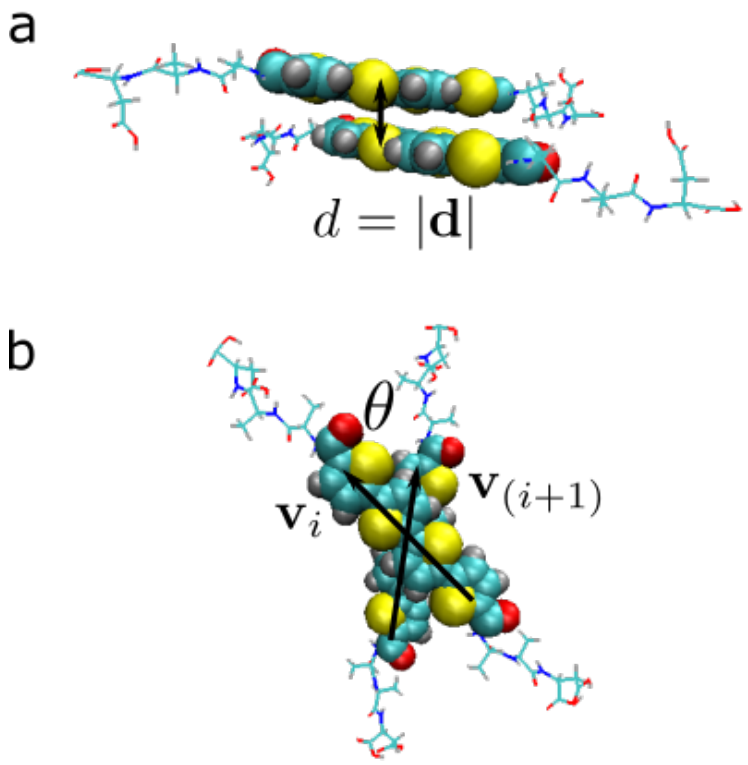

Figure 2: Schematic of an OT4 dimer illustrating the definition of the dimer separation d and twist angle θ in a right-handed convention.

Hoover thermostat with a time constant of 0.5 ps, and a Parrinello-Rahman barostat with a time constant of 1.0 ps were used.[72–75] Histograms of the center-of-mass separation and relative twist angles between neighboring peptides were collated over the terminal 10 ns of the production run for each of the five oligopeptides. A representative molecular rendering, constructed using VMD,[76] of the stack of 20 DAA-OT4-AAD oligopeptides at the end of the 150 ns simulation is presented in Fig. 3.

Density functional theory calculations

The MD simulations contain upwards of 2,000 oligopeptide atoms and 10,000 solvent atoms, placing them well outside the reach of quantum-mechanical electronic-structure calculations. We instead extract the distributions of the center-of-mass separation and relative twist angle between neighboring oligopeptides from our MD simulations and use these to inform an

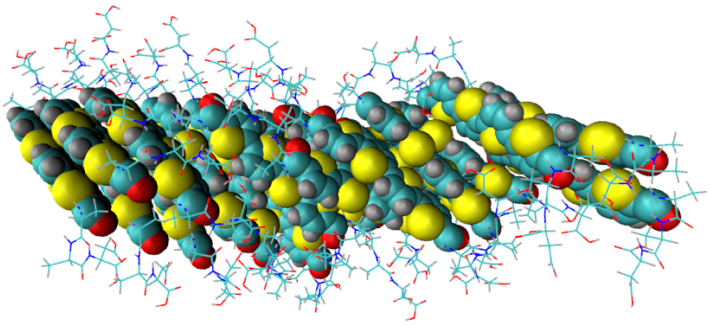

Figure 3: Snapshot of the relaxed stack of 20 DAA-OT4-AAD oligopeptides after a 150 ns molecular dynamics simulation. The atoms comprising the OT4 cores are rendered as space-filling van der Waals spheres, and the DAA peptide wings in line representations. C atoms are colored cyan, H white, O red, N blue, and S yellow. The values of d and θ observed in MD simulations of a 1D stack of 20 DXX-OT4-XXD peptides are used to inform DFT calculations on OT4 dimers to calculate absorption spectra as a function of dimer geometry.

ensemble of DFT calculations on pairs of quaterthiophene cores. Specifically, we manually constructed dimers at particular values of the dimer separation d and twist angle θ by placing a pair of extended oligopeptide monomers into the desired dimer geometry. We considered ranges of d and θ observed in the MD simulations. This protocol provides us with precise control over the dimer geometry without the confounding influences of additional structural heterogeneity and allows us to cleanly resolve trends in the electronic and optical properties associated with changes in d and θ. This is similar to the approach followed by Würthner, Engels, and coworkers who computed emission and absorption spectra and ground and excited state potential energies for perylene bisimide dimers as a function of dimer geometry.[77,78] In sum, we constructed quaterthiophene dimers at a variety of center-of-mass separations and relative twist angles informed by the classical MD simulations and then computed absorption spectra from first principles.

Focusing on quaterthiophene (OT4) dimers comprising only 60 atoms renders these calculations computationally tractable, but doing so makes four primary assumptions. First, since the hydrophobic OT4 cores lie sequestered from water in the core of the 1D nanoaggregates, we assume that the effect of the water solvent on the absorption spectrum may

be neglected. This simplifying assumption allows us to neglect the solvent and renders tractable large ensembles of DFT calculations conducted at a variety of dimer separations and twist angles. Future work on a more restricted number of dimer configurations may better represent solvent using either an implicit (e.g., COSMO[79] or PCM[80]) or fully explicit treatment.

Second, we assume that the optical response is governed primarily by electronic transitions within the π-conjugated cores and does not involve the peptide wings. This amounts to assuming that the experimentally observed differences in the optical response for different DXX oligopeptides is due to the different structural arrangements the X amino acids induce between the π cores and not due directly to the differential optical properties of the amino acids themselves. This assumption is consistent with experimental measurements on DXX-OT4-XXD monomers showing the absorption and emission spectra to be invariant to the choice of X = {A, F, G, I, V}.[29] Our tests of this assumption show that the calculated absorption spectra of these five monomers are qualitatively similar; at the onset of absorption, the spectra consist of a single peak with centers between 699 nm and 744 nm with full widths at half maxima of $\sim$70 nm. Removal of the peptide wings and carbonyl linkers to leave just the quaterthiophene cores produces a $\sim$60 nm blue-shift without changing the spectral shape. This blue shift is not unexpected since removal of the amides decreases the overall conjugation of the oligothiophene.

Third, it is assumed that the absorption spectra computed for peptide dimers are representative of those for the micron-long 1D oligopeptide nanoaggregates.[29] If electronic transitions were restricted to nearest neighbors in the peptide stacks this approximation would be exact. Unfortunately, the rapidly increasing expense of the DFT calculations with number of oligopeptides makes it computationally intractable to directly validate this hypothesis. Instead we pursue this reductionist approach to compare changes in the absorption spectrum as a function of dimer orientation to ascertain changes in the absorption spectrum at the level of dimers. In this manner, we seek fundamental insight into the structural dependence

of the absorption spectrum upon dimer orientation, but do not seek to quantitatively reproduce the experimentally measured spectra. Support for this assumption is provided by the work of Würthner, Engels, and coworkers who demonstrated the experimentally measured absorption and emission spectra of perylene bisimide dye aggregates to be predicted with high fidelity from computational models of dimers and trimers.[77,78]

Fourth, we compute spectra using DFT on unrelaxed atomic geometries. The use of unrelaxed molecular structures is intended to better mimic the finite-temperature peptide structures as opposed to energy-relaxed idealizations. The use of DFT ignores one- and two-quasiparticle effects on the optical spectra, leading to band-gap underestimation and neglect of excitonic effects. However, for this work the use of DFT, as opposed to a higher level of theory, is beneficial since it renders these calculations computationally tractable for large ensembles of dimer configurations. In addition, the independent-particle approximation allows straightforward decomposition of spectra into atomic and orbital contributions. Further, we verified that the electronic energy levels of the monomer computed employing unrelaxed molecular structures are indistinguishable from those employing relaxed structures within the 0.1 eV bandwidth of the Gaussian smoothing kernel with which the line spectra are convolved to produce the dielectric function.

First-principles DFT simulations were performed using the Vienna *Ab-Initio* Simulation Package[81,82] (VASP) with the projector-augmented wave (PAW) method[83] to describe the electron-ion interaction. The generalized-gradient approximation (GGA) of Perdew, Burke, and Ernzerhof (PBE)[84] was used to approximate electron exchange and correlation effects. Kohn-Sham wave functions are expanded into a plane-wave basis with a kinetic-energy cutoff of 550 eV. Molecules are simulated in a periodic cell with dimension $30 \times 30 \times 30$ Å^3, to eliminate artificial interactions between periodic images. This large cell justifies using only the Γ point for Brillouin zone sampling.

We then study optical properties, using the complex frequency-dependent dielectric tensor in independent-particle approximation. The Ehrenreich-Cohen formula in the optical limit of

vanishing wave vectors q, to account for vertical electronic transitions in optical absorption, yields for the imaginary part of this tensor[85]

$$\epsilon_2^{\alpha\beta}(\omega) = \frac{4\pi^2 e^2}{\Omega} \lim_{q\to 0} \frac{1}{q^2} \sum_{c,v,\mathbf{k}} 2w_{\mathbf{k}} \delta(\varepsilon_{c,\mathbf{k}} - \varepsilon_{v,\mathbf{k}} - \hbar\omega) \times \langle u_{c,\mathbf{k}+\mathbf{e}^\alpha\mathbf{q}} | u_{v,\mathbf{k}} \rangle \langle u_{c,\mathbf{k}+\mathbf{e}^\beta\mathbf{q}} | u_{v,\mathbf{k}} \rangle^* . \tag{1}$$

Here, $\mathbf{q}$ is the vector describing the electron momentum change, $w_{\mathbf{k}}$ is the symmetry weight of each $\mathbf{k}$ point, and $u_{v,\mathbf{k}}$ is the periodic part of the Bloch wave function for band v at $\mathbf{k}$. Indices c and v run over the conduction and valence bands, respectively, and $\mathbf{e}^\alpha$ are the Cartesian unit vectors.[85] As is conventional practice, all of the dielectric functions presented henceforth are generated by convoluting calculated line spectra with a Gaussian smoothing kernel of bandwidth 0.1 eV to produce continuous spectra.

The real part of this tensor is obtained via the Kramers-Kronig transformation,

$$\epsilon_1^{\alpha\beta}(\omega) = 1 + \frac{2}{\pi} P \left(\int_0^\infty \frac{\epsilon_2^{\alpha\beta}(\omega')\omega'}{\omega'^2 - \omega^2} d\omega' \right) . \tag{2}$$

From Eqs. (1) and (2), the real and imaginary parts of the complex refractive index follow as

$$n = \frac{1}{\sqrt{2}} \left(\epsilon_1 + (\epsilon_1^2 + \epsilon_2^2)^{\frac{1}{2}} \right)^{\frac{1}{2}} , \tag{3}$$

$$\kappa = \frac{1}{\sqrt{2}} \left(-\epsilon_1 + (\epsilon_1^2 + \epsilon_2^2)^{\frac{1}{2}} \right)^{\frac{1}{2}} . \tag{4}$$

The optical-absorption spectrum is then calculated straightforwardly as $\alpha = \frac{4\pi\kappa}{\lambda}$.

Finally, while absorption is a readily measurable quantity, we also analyze ion-resolved

contributions to molecular absorption by means of the ion-projected dielectric function,

$$\epsilon_2^{\alpha\beta}(\omega) = \frac{4\pi^2 e^2}{\Omega} \lim_{q\to 0} \frac{1}{q^2} \sum_{M,N} \sum_{c,v,\mathbf{k}} 2w_{\mathbf{k}} \delta(\varepsilon_{c,\mathbf{k}} - \varepsilon_{v,\mathbf{k}} - \hbar\omega) \times p_c^M p_v^N \left(\langle u_{c,\mathbf{k}+\mathbf{e}^\alpha \mathbf{q}} | u_{v,\mathbf{k}} \rangle \langle u_{c,\mathbf{k}+\mathbf{e}^\beta \mathbf{q}} | u_{v,\mathbf{k}} \rangle^* \right). \tag{5}$$

The indices M and N run over all atoms in the dimer and the projections p_i^M are computed from summing the square of the overlaps between spherical harmonic functions centered on ion M and the electron wave functions. The subscripts c and v indicate that the projection is performed on conduction or valence states, respectively. In isolated molecules, the sum reduces to inclusion of a single electronic wavevector at the Γ-point, $\mathbf{k} = \mathbf{0}$.

All relevant input and output files for generating figures in this paper can be found in the Materials Data Facility.[86–88]

Results and Discussion

Amino acid substitutions control the stacking of OT4 cores

Consistent with simple energy-minimized molecular models of DXX-OT4-XXD stacks[29] and prior MD simulations of DXXX-π-XXXD oligopeptides with dimeric and trimeric oligo(p-phenylenevinylene) π-conjugated cores,[12,36] we find that amino acid substitutions proximate to the π subunit strongly affect the structural arrangements of the cores. The distribution of center-of-mass spacings for the five peptides all lie in the range of 0.40 – 0.55 nm (Fig. 4a). To contextualize these values, we note that an intermolecular spacing of ∼0.35 nm is considered the idealized value for π-π stacking interactions[77,89] whereas ∼0.50 nm is typical of natural β-sheets.[90] Ala is an outlier among the five amino acid substitutions that results in ∼10% closer center-of-mass separations. This tighter packing is consistent with experimental observations of DAA-OT4-AAD as an outlier among the five oligopeptides in producing wider self-assembled nanoaggregates.[29]

The relative twist angles between neighboring oligopeptides follow approximately Gaussian distributions for each of the five oligopeptides lying in the range $0-25^\circ$ (Fig. 4b). Consistent with observations from energy-minimized DXX-OT4-XXD structures,[29] the Ile and Val substitutions that possess strong preferences for β-sheet secondary structure formation produce stacks with modal twist angles of 18.7° and 19.2° that approach the $\sim 25^\circ$ value for natural β-sheets.[90,91] The Phe substitution results in a slightly smaller most probable twist angle of 15.3°, but shows substantial overlap with the Ile and Val distributions. The two sterically smallest amino acids Gly and Ala exhibit twist angle distributions with modal values of 10.7° and 5.0°. This is consistent with prior observations that small residues produce the largest deviations from ideal β-sheet-like stacking, and exhibit significantly blue-shifted absorption spectra relative to bulkier amino acids.[29] In gross terms, the three bulky sequences DFF, DII, and DVV produce aggregates with mean relative twist angles in excess of 15° and approaching the 25° value for ideal β-sheets, whereas the two smaller amino acid substitutions DAA and DGG produce stacks with mean angles of 10° or less that approach the 0° limit of linear stacks.

Optical transitions

With the wings removed, absorption spectra of OT4 dimer cores depend on the intermolecular spacing and relative twist between molecules. Fig. 5 visualizes absorption spectra for three interchain separations with twist angles ranging from 0° to 90° in increments of 5°. We recall that the MD simulations showed dimer spacings to lie in the range d=0.40 – 0.55 nm, and twist angles in the range θ=$0-25^\circ$.

For separations of 0.45 nm and 0.75 nm at all twist angles, the primary absorption peak occurs at 650 nm. At wavelengths shorter than about 350 nm, high-energy continuum absorption out of occupied states sets in. In the case of 0.35 nm separation, the first absorption peak occurs at 650 nm only for twist angles between 0° and 55°. At larger twist angles, the main absorption peak splits into two. No features in the absorption spectra are observed

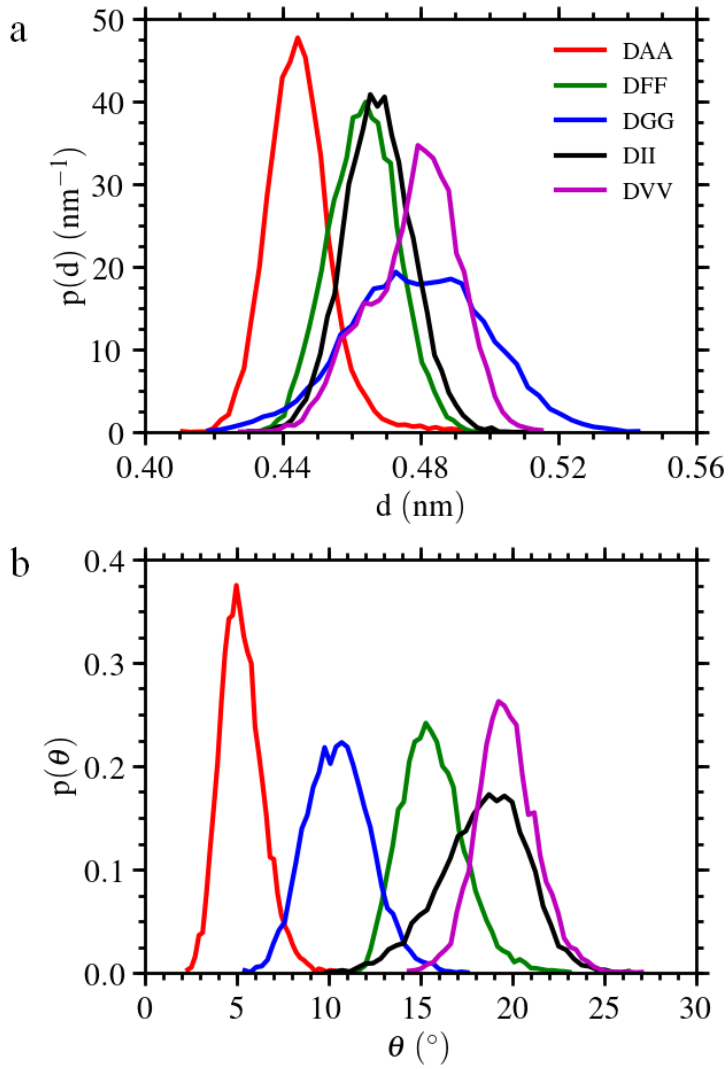

Figure 4: Probability density functions of the distribution of (a) center-of-mass separations and (b) relative twist angles between neighboring oligopeptides computed from MD simulations of relaxed stacks of 20 DXX-OT4-XXD oligopeptides. We observe tighter packing in DAA oligopeptides and smaller twist angles for DGG and DAA oligopeptides. No correlation between separation and twist angle is found.

for wavelengths longer than 800 nm. To better understand the absorption spectra of dimer chains, energy levels represented by DFT-PBE Kohn-Sham eigenvalues are plotted in Fig. 6. We also use wavelengths and oscillator strengths of the possible optical transitions between these levels plotted in Fig. 7 to help explain the observed trends.

The energy levels for configurations with an interchain spacing of d=0.75 nm are independent of twist angle θ (Fig. 6c). The absorption peak at 650 nm in Fig. 5c corresponds

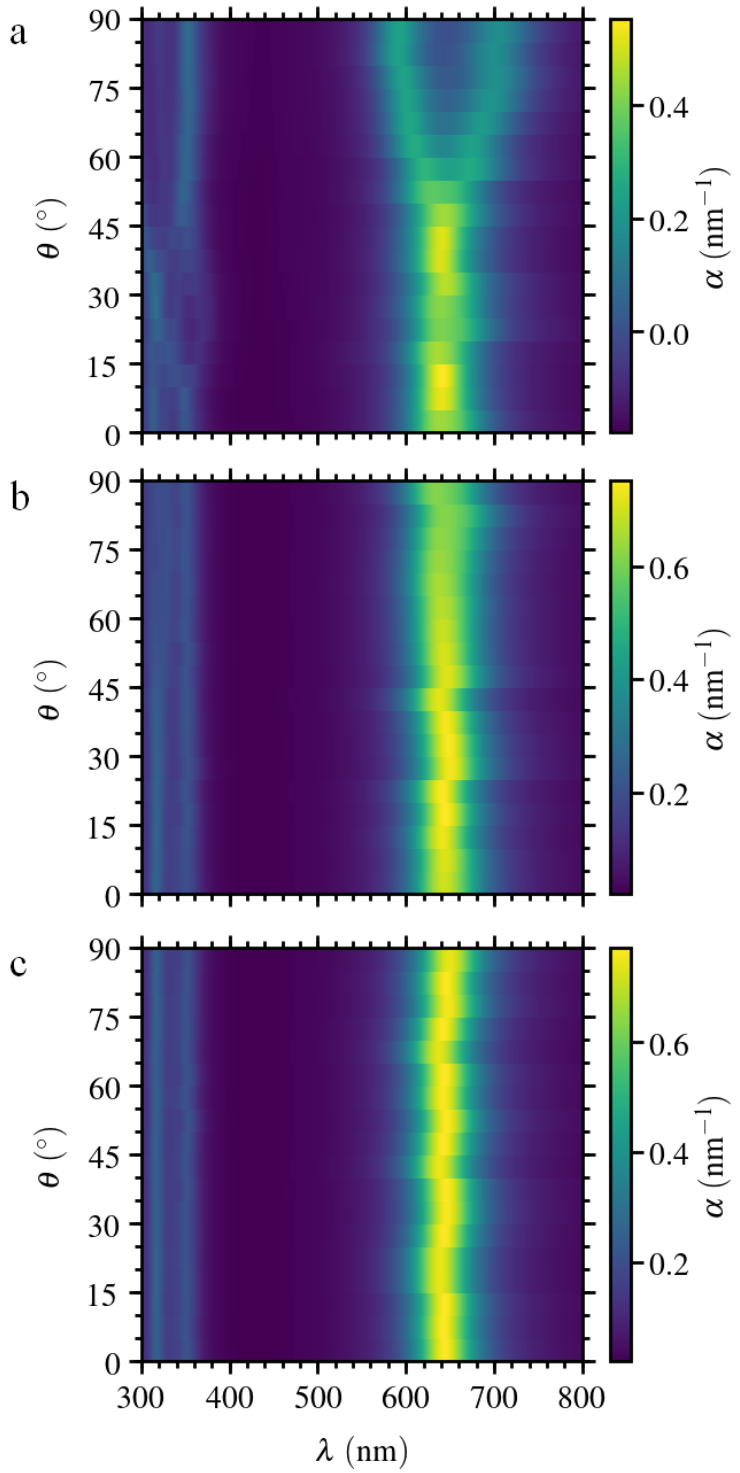

Figure 5: Calculated absorption α (in nm^{-1}) as a function of wavelength λ (in nm) and relative twist angle θ for an OT4 dimer with interchain spacings d of (a) 0.35 nm, (b) 0.45 nm, and (c) 0.75 nm.

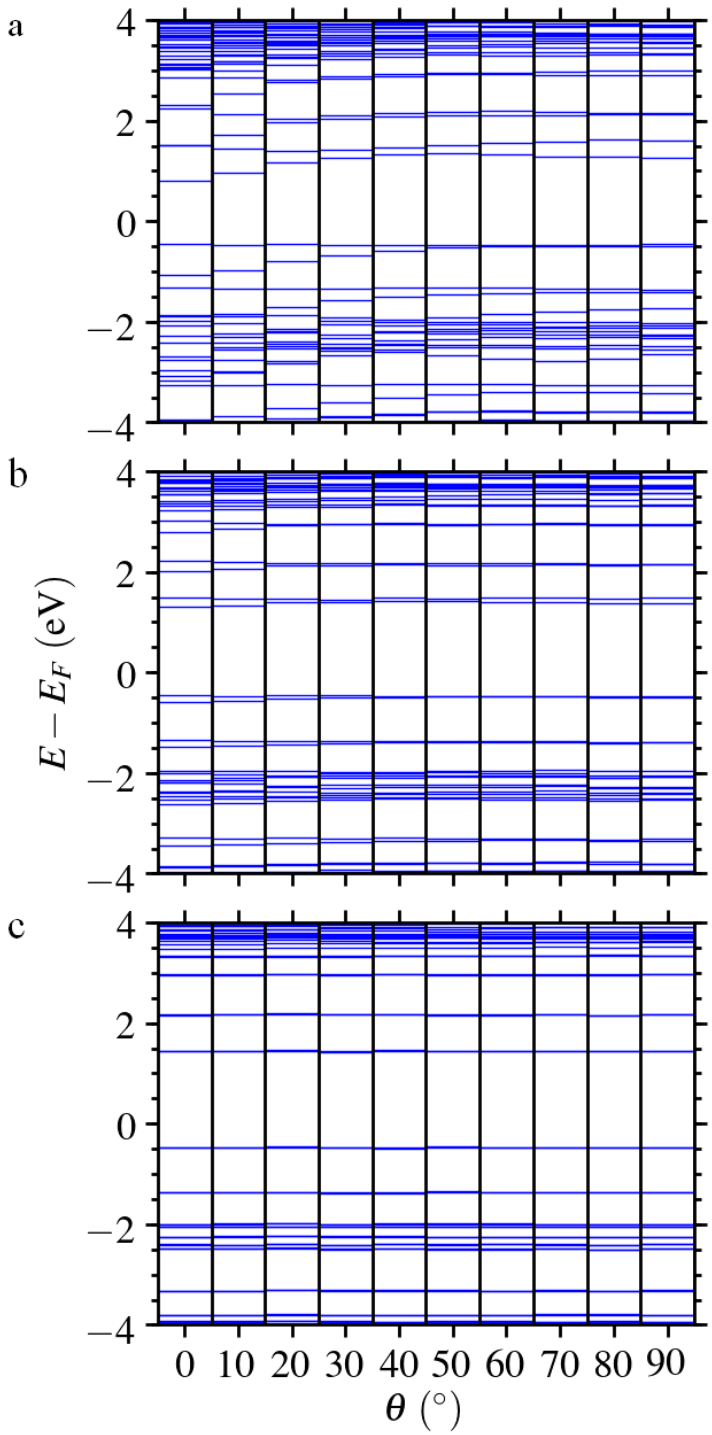

Figure 6: OT4 dimer energy levels $E - E_{\mathrm{F}}$ computed within DFT-PBE as a function of relative twist angle θ at interchain spacings d of (a) 0.35 nm, (b) 0.45 nm, and (c) 0.75 nm.

to the energy difference between the highest occupied molecular orbital (HOMO) and the lowest unoccupied molecular orbital (LUMO), calculated as 1.91 eV. Fig. 7c shows that the

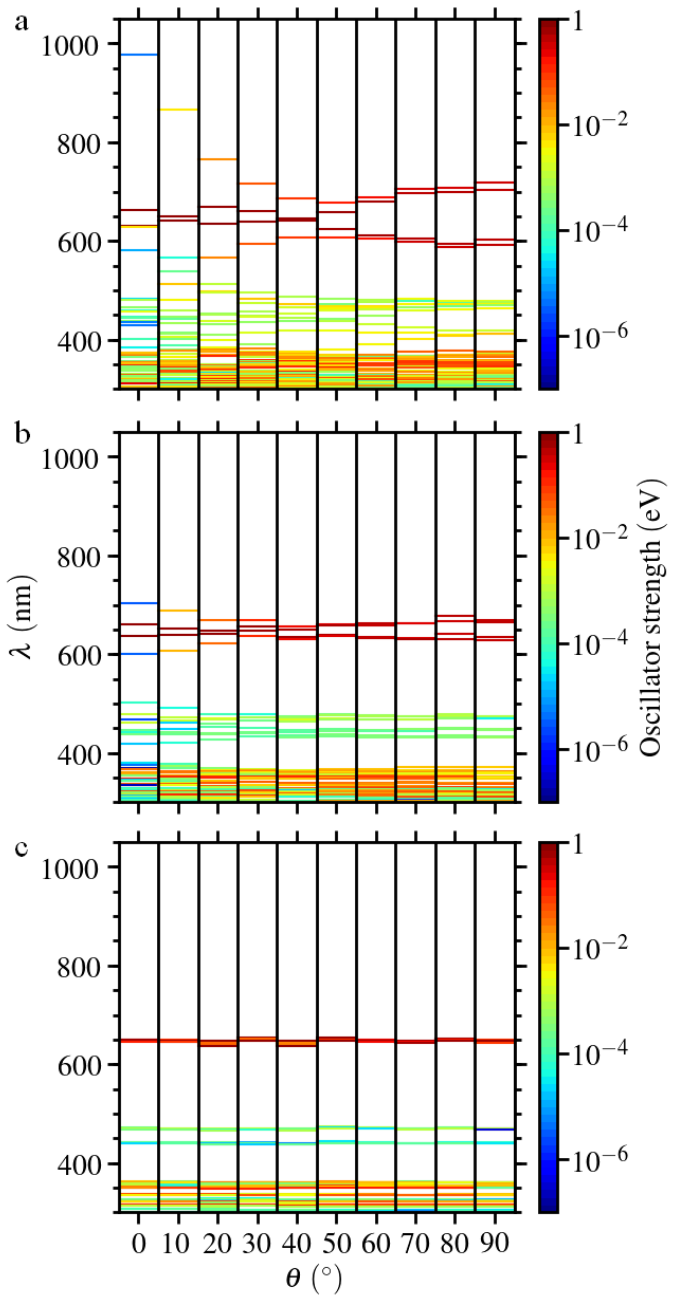

Figure 7: Wavelengths and oscillator strengths of the possible optical transitions for the OT4 dimer as a function of twist angle θ at interchain spacings d of (a) 0.35 nm, (b) 0.45 nm, and (c) 0.75 nm. The positions of the horizontal lines derive from DFT-PBE Kohn-Sham eigenvalue differences for each transition. The line color indicates the strength of the transition; colors toward the red end of the spectrum correspond to more probable transitions.

wavelengths and oscillator strengths of the possible transitions are largely independent of the twist angle.

For the dimer with a separation of d=0.45 nm and twist angle of θ=0° shown in Fig. 6b, the HOMO-LUMO energy difference is 1.76 eV, corresponding to a wavelength of 704 nm. While there is no corresponding feature at this wavelength in the absorption spectrum in Fig. 5b, this can be explained by the very low oscillator strength of the corresponding optical transition. Fig. 7 illustrates the very small optical oscillator strength at this wavelength, rendering it difficult to observe in the optical-absorption spectrum. The transition between the electronic level below the HOMO (next HOMO, NHOMO) and the LUMO has an energy of 1.88 eV (660 nm) and the transition between the HOMO and next lowest unoccupied molecular orbital (next LUMO, NLUMO) has an energy of 1.95 eV (635 nm) for θ=0°. The energy difference between the HOMO and the NHOMO decreases from 0.07 eV to 0.01 eV as the twist angle increases to 50° (Fig. 6b). This is accompanied by a change of the character of these levels. For small twist angles, HOMO and NHOMO correspond to electronic states that span C atoms in both molecular chains; for larger twist angles the chains interact less, the energy levels become closer, and NHOMO and HOMO are each localized almost entirely on alternate chains. For the LUMO and NLUMO, the energy difference is between 0.07 eV at 50° and 0.18 eV at 0°. This weak dependence of the energy levels on the twist angle explains the relatively constant wavelength of the absorption peak for all twist angles θ at a separation of d=0.45 nm. Furthermore, Fig. 7b shows that at least two transitions with large oscillator strength contribute to the absorption peak around 650 nm, however, the wavelength of the first transition varies by only 40 nm over the twist angle range θ=0 – 90° and the splitting is small. Hence, the broadening used in calculating the absorption spectrum obscures the split character of the electronic states and they appear as a single peak in Fig. 5b.

Finally, for the dimer with a separation of d=0.35 nm – the idealized spacing for π-π stacking interactions[77,89] – and twist angle of θ=0° shown in Fig. 6a, there is a HOMO-LUMO transition energy of 1.27 eV (978 nm). As with the d=0.45 nm configurations, no

corresponding absorption peak is observed at this wavelength in Fig. 5a and from Fig. 7a it becomes clear that this can again be attributed to the small optical oscillator strength of this transition. For twist angles of $\theta < 20°$, the oscillator strength of the longest wavelength transition remains four orders of magnitude lower than the second and third longest wavelength transitions. Consequently, the first transition may not be observed through the absorption spectrum or dielectric function.

As the twist angle increases in the d=0.35 nm dimer, the wavelength of this first transition decreases by as much as 300 nm (Fig. 7a), approaching 700 nm at θ=60° while the oscillator strength increases by four orders of magnitude to become comparable to that of the second and third transitions. For high twist angles, this first transition thus does contribute to the absorption onset and Fig. 7a even shows that, in total, four optical transitions in a small energy range determine the onset of the absorption spectrum at intermediate and high twist angles. Fig. 6a illustrates a strong twist angle dependence of these states and we attribute this to strong interactions between both molecules for a separation of d=0.35 nm. The change in electronic character of these states is similar to that discussed for d=0.45 nm.

For a twist angle of θ=90° in the d=0.35 nm dimer, the HOMO and NHOMO differ by 0.03 eV, while the LUMO and NLUMO differ by 0.33 eV, see Fig. 6c. In contrast, for θ=0°, HOMO and NHOMO differ by 0.60 eV, while LUMO and NLUMO differ by 0.70 eV. Consequently, transition energies (wavelengths) between these states are 1.73 eV (718 nm), 1.76 eV (704 nm), 2.06 eV (602 nm), and 2.09 eV (592 nm) at θ=90° and 1.27 eV (978 nm), 1.87 eV (662 nm), 1.97 eV (632 nm), 2.57 eV (483 nm) at θ=0°. At θ=0°, therefore, there are two additional transitions with energies lower than 2.57 eV, invoking HOMO and the level above the NLUMO, 1.98 eV (627 nm), and LUMO and the level below the NHOMO, 2.13 eV (581 nm). This analysis allows us to attribute the absorption peak at 650 nm for θ=0° in Fig. 5a to a pair of transitions with large optical oscillator strength (Fig. 7a) and their energy dependence explains the splitting of this peak for large twist angles $\theta > 55°$. With a twist angle of θ=90°, the shorter wavelength member of the split peak can be attributed

to the 2.06 eV (602 nm) and 2.09 eV (592 nm) transition pair, and the longer wavelength member to the 1.73 eV (718 nm) and 1.76 eV (704 nm) pair.

Orbital contributions to optical response

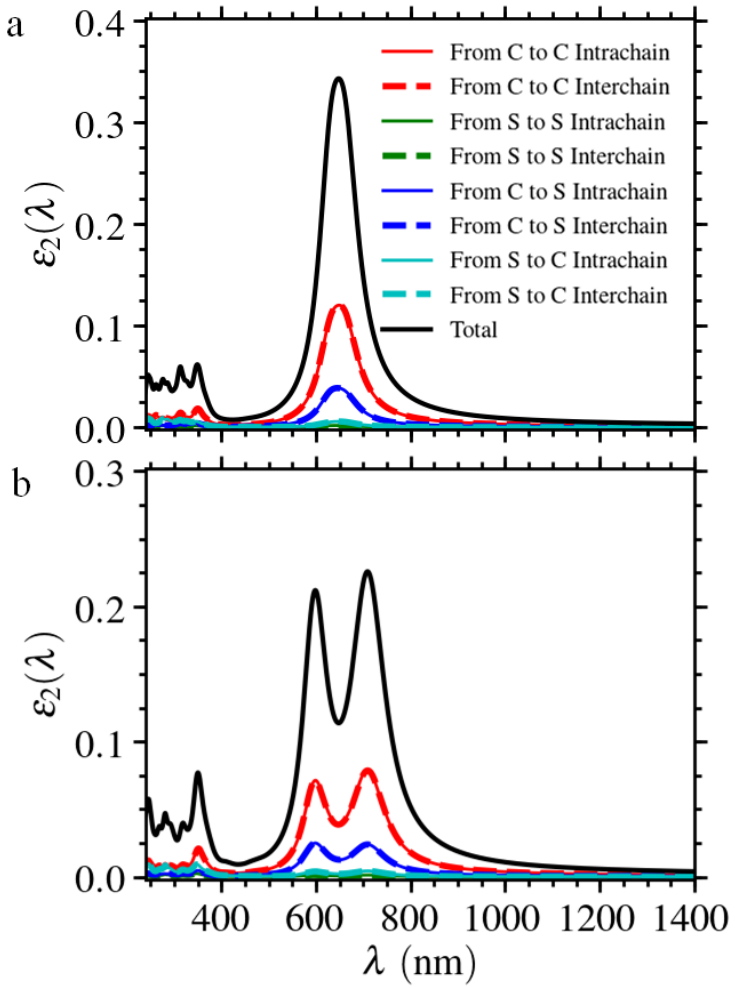

Figure 8: Ion-projected imaginary part of the dielectric function ϵ_2 as a function of wavelength λ at a dimer separation of d=0.35 nm and a twist angle θ of (a) 0° and (b) 90°.

To resolve the origin of the trends in the absorption spectra as a function of dimer separation and twist angle, we decomposed the absorption spectra into atomic contributions using the ion-projected dielectric function in Eq. (5). Fig. 8 plots the dielectric function projected by atomic species and interchain versus intrachain contributions for d=0.35 nm and twist angles of θ=0° and 90°. In both configurations, the primary peaks between 400

nm and 800 nm in the dielectric function are dominated by excitations of electrons from C $2p$ to C $2p$ orbitals, with interchain and intrachain contributions approximately equal. After C to C transitions, the next leading contributions are due to C $2p$ to S $3p$ transitions.

This is consistent with the partial densities of states at twist angles of θ=0° and 90° at d=0.35 nm (Fig. 9a,b) and d=0.45 nm (Fig. 9c,d). In all cases, the densities of states of valence and conduction bands from 3.5 eV below the Fermi energy to 3.5 eV above the Fermi energy are dominated by electronic states composed of C $2p$ and S $3p$ orbitals. For conduction states, the S $3p$ contributions are found to be as large as 35%. The peak splitting at 1.9 eV (650 nm) observed for twist angles $\theta > 55°$ at d=0.35 nm can be attributed to splitting of these p-orbitals (see arrows in Fig. 9a,b).

Charge localization and optically induced charge transfer

In order to study charge localization in the ground state and to probe charge transfer between molecules in the dimer upon optical excitation, we plot the HOMO and LUMO partial electron density for four representative dimer configurations. For a dimer at a twist angle of θ=0° (Fig. 10) and θ=90° (Fig. 11) we plot corresponding isosurfaces for intermolecular separations of d=0.35 nm and d=0.45 nm. At the smaller twist angle where the molecules are linearly stacked we observe approximately equal sharing of electron density between the two chains for both the HOMO and LUMO at both d=0.35 nm (Fig. 10a,b) and d=0.45 nm (Fig. 10c,d). At the smaller interchain separation there is an elevated overlap of the orbitals from both chains and increased electron density in the region between the chains compared to larger separations. The LUMO at a separation of 0.35 nm possesses an isosurface that spans the atoms in both chains (Fig. 10b) whereas at the larger separation these isosurfaces disconnect, which illustrates the lower charge density in the interchain region (Fig. 10d). At this small twist angle, excitation of an electron from the HOMO into the LUMO maintains the approximately equal sharing of the electron density between the chains. We also see that the excitation leads to delocalization of charge, as indicated by the more extended LUMO

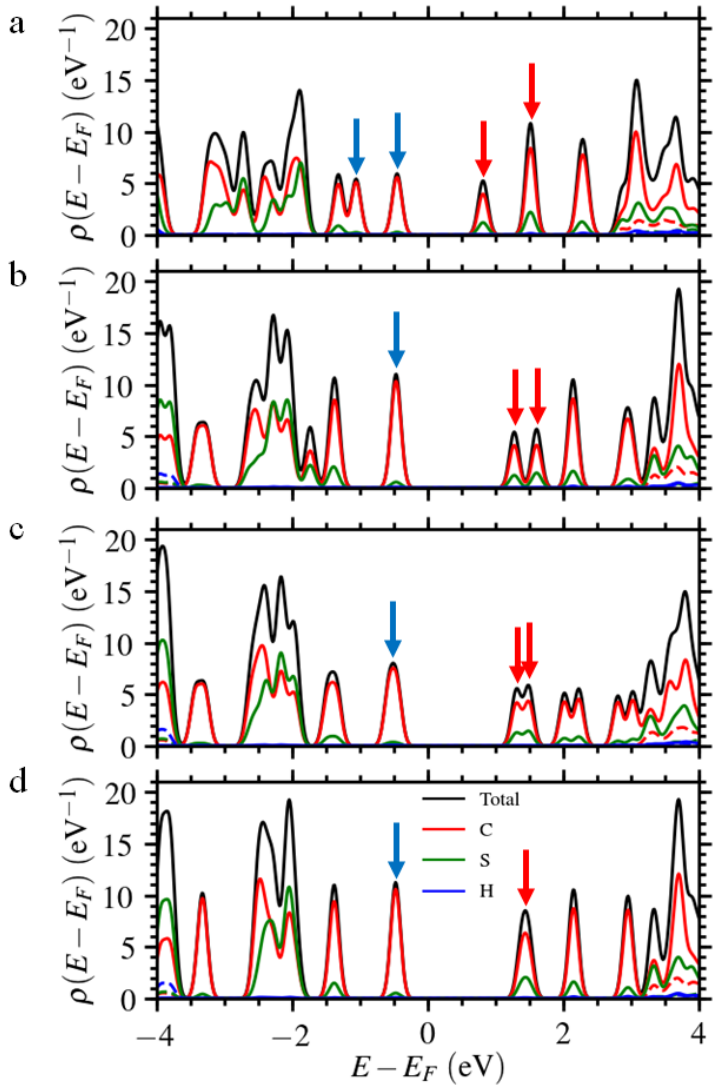

Figure 9: Density of states $\rho(E - E_F)$ projected on atomic species and orbital angular momentum contributions for (a) $d = 0.35$ nm, $\theta = 0°$, (b) $d = 0.35$ nm, $\theta = 90°$, (c) $d = 0.45$ nm, $\theta = 0°$, and (d) $d = 0.45$ nm, $\theta = 90°$. Solid curves correspond to p orbitals while dashed lines correspond to s orbitals. Blue arrows indicate peaks corresponding to the NHOMO and HOMO and red arrows indicate the LUMO and NLUMO. If the levels are too close to resolve, only a single arrow is shown.

partial electron density.

In the θ=90° perpendicular arrangement (Fig. 11), HOMO and NHOMO are energetically close bands (energy separation is 0.03 eV for d=0.35 nm and 0.02 eV for d=0.45 nm), each of which corresponds to electron density localization on one of the two chains. We plot the HOMO as one of the bands for separations of 0.35 nm and 0.45 nm in Fig. 11a and

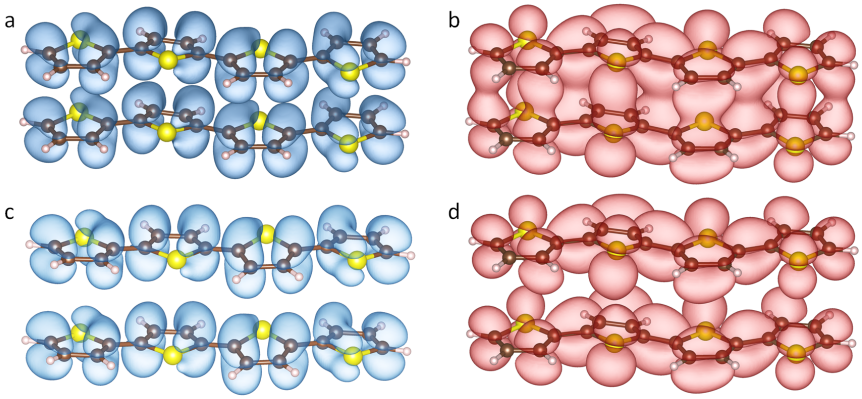

Figure 10: HOMO and LUMO partial electron density isosurfaces (containing 90% of the density) for dimer pairs at a twist angle of θ=0°. (a) HOMO and (b) LUMO at an interchain separation of d=0.35 nm. (c) HOMO and (d) LUMO at an interchain separation of d=0.45 nm.

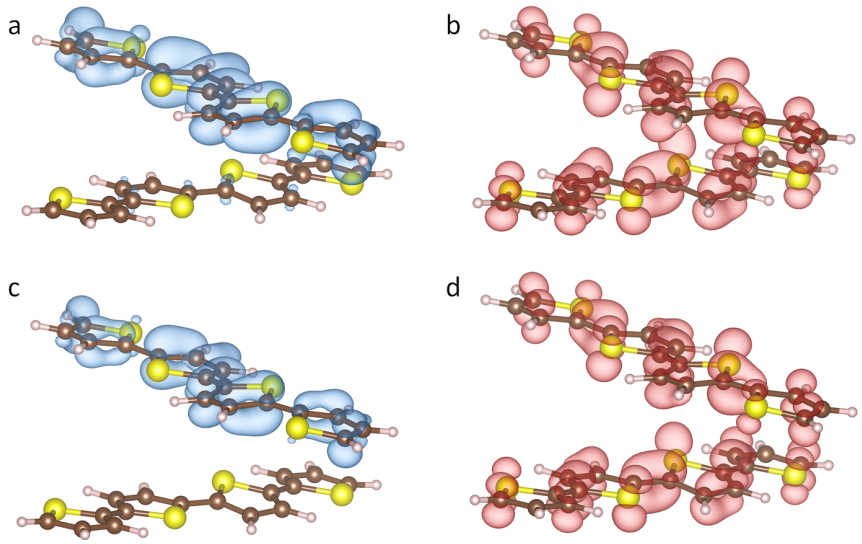

Figure 11: HOMO and LUMO partial electron density isosurfaces (containing 90% of the density) for dimer pairs at a twist angle of θ=90°. (a) HOMO and (b) LUMO at an interchain separation of d=0.35 nm. (c) HOMO and (d) LUMO at an interchain separation of d=0.45 nm.

c; the NHOMO is localized on the opposite chain. As expected, the degree of asymmetry in the electron density localization, quantified by orbital projections, increases with chain separation, resulting in nearly complete localization on one of the two chains at the larger separation considered. Turning to the LUMO in Fig. 11b and d, we observe that excitation of an electron into this orbital results in equal sharing of electron density between the two

chains comprising the dimer.

Comparison of the partial electron densities between both twist angles (Fig. 10 vs. Fig. 11) shows that for the 0° configuration, HOMO and LUMO extend more out of the molecular plane, connecting the two chains. In contrast, HOMO and LUMO for the 90° configuration are more localized on the individual chains, with the electron density not extending much out of the molecular plane.

Summary and Conclusions

We employed all-atom classical MD simulations to determine the structural arrangement of OT4 π-conjugated cores within self-assembled aggregates of DXX-OT4-XXD oligopeptides. Our primary findings are that the proximity and relative angle between OT4 cores are perturbed by the identity of the X residue in the DXX peptide wings, with bulkier residues correlated with larger relative twist angles. Specifically, the MD data shows that the five oligopeptides considered here partition into two groups, with the smaller DAA and DGG oligopeptides producing small mean relative twist angles less than $\sim$10°, and the bulkier DFF, DII, and DVV oligopeptides resulting in angles exceeding $\sim$15°. This split is in line with the experimentally observed grouping in which DAA and DGG aggregation results in a $\sim$50 nm blue-shift in the absorption spectrum peak, whereas DFF, DII, and DVV produce only a $\sim$10 nm blue-shift.[29] Across these five oligopeptides we observe dimer separations of d=0.40 – 0.55 nm and relative twist angles of θ=0 – 25°. These distributions informed ensembles of DFT calculations of the absorption spectra of OT4 dimers as a function of separations over the range $d = 0.35 - 0.75$ nm and relative twist angles over the range $\theta = 0 - 90°$ to understand the optical implications of different OT4 core separations and orientations induced by the different amino acid identities in the peptide wings.

In terms of absorption spectra, our DFT calculations revealed the spectra to be insensitive to twist angle at interchain separations of $d \geq 0.45$ nm, possessing a primary absorption

peak at λ=650 nm. At smaller separations we observed splitting of the primary peak into a pair of peaks at λ=600 nm and λ=700 nm for twist angles $\theta > 55°$. Analysis of the transition energies and oscillator strengths revealed the origin of the splitting to be due to p orbital hybridization and subsequent grouping of transition energies into two pairs with high oscillator strength that manifest as a pair of peaks due to energetic smearing. We showed that this grouping can be traced back to the fact that the HOMO and NHOMO energy converge to close to the same value for large twist angles, while the LUMO and NLUMO energies are different. Projecting wave functions onto atomic orbitals shows the molecular absorption spectrum to be dominated by transitions from C $2p$ orbitals to C $2p$ and S $3p$ orbitals, with nearly equal contributions from interchain and intrachain transitions at small interchain separations of d=0.35 nm.

Our classical mechanical calculations on 20 oligopeptide monomers conducted herein have shown the DXX-OT4-XXD peptides to form stacks with inter-peptide separations of $d \approx 0.45$ nm. Less sterically bulky X residues (X = G, A) produce linear-like stacks with mean twist angles of θ=5 – 10°, whereas more bulky residues (X = F, I, V) produce more twisted stacks with mean twist angles of θ=15 – 20°. Our DFT calculations reveal that the absorption spectrum of the dimer at an inter-peptide separation of $d \approx 0.45$ nm to be largely invariant to the twist angle θ. Experimental absorption spectra reveal a peak at $\lambda \approx 360$ nm for DAA and DGG compared to $\lambda \approx 410$ nm for DFF, DII, and DVV.[29] The twist-angle dependence of our calculated absorption spectra for dimers of OT4 cores do not reproduce this trend: the spectra of dimers at DAA and DGG twist angles of θ=5 – 10° are indistinguishable from those at DFF, DII, and DVV twist angles of θ=15 – 20°. Accordingly, we posit that the experimentally observed spectral shifts are due to multi-peptide electronic effects that cannot be captured at the level of the dimer. In future work, we propose to extend our DFT calculations to multimeric stacks of several oligopeptides constructed in defined geometries and extracted directly from our MD simulations. These (expensive) calculations will explicitly test the hypothesis that electronic interactions within multimeric

stacks are responsible for the experimentally observed peak shifts.

In terms of electron density distributions, our DFT calculations show that for both peptides within the dimer, relative energies and degree of asymmetry in the electron density for states near the gap are a strong function of twist angle and interchain separation. Considering the HOMO and LUMO as a function of dimer geometry, we observe approximately equal sharing of electron density between both molecular chains for HOMO and LUMO at interchain separations of d=0.35 – 0.45 nm and small twist angles, corresponding to an approximately linear stacking arrangement. For these small θ and small d dimer configurations, there is also an energy difference between the NHOMO and HOMO and a near equal distribution of NHOMO and HOMO electronic density between the two molecules. The larger the interchain separation d, the smaller the energy differences between the NHOMO and HOMO as well as between the LUMO and NLUMO, until each pair of bands becomes degenerate. At twist angles of $\theta = 65°$, the NHOMO and HOMO are nearly degenerate (energy difference of 0.015 eV for d=0.35 nm and 0.004 eV for d=0.45 nm), with each state localizing density on opposite molecules. Finally, at a twist angle of θ=90°, corresponding to perpendicular stacking arrangements, the NHOMO and HOMO are more localized on individual molecular chains of the dimer, and have a small but finite energy difference of 0.03 eV for d=0.35 nm and 0.02 eV for d=0.45 nm. The increase in HOMO-NHOMO energy difference indicates a lifting of the near-degerneracy observed at $\theta = 65°$ as the twist angle is increased to $\theta = 90°$.

These results have important implications for understanding the optical and charge transfer properties in 1D self-assembled stacks of π-conjugated oligopeptides. In particular, at large twist angles there is large asymmetry in the electron distribution of the NHOMO and HOMO, with the preponderance of the density localized on one molecule. The consequences of this result for electronic delocalization and charge transfer and transport processes are as follows. Linear-like alignment of the oligopeptides favors electronic delocalization over the two molecules constituting the dimer. Although multimeric calculations would be required to explicitly test this assertion, extrapolating our results to stacks of multiple peptides suggest

that good alignment between neighboring peptides at small twist angles θ would be required for electronic delocalization over the stack of molecules. Sterically less bulky residues (X = A, G) favor more linear stacking arrangements and are therefore predicted to give rise to better delocalization over self-assembled nanoaggregates of these oligopeptides compared to those containing bulkier X = F, I, V substitutions. Furthermore, our results suggest that single perpendicular twist angles that may exist as stacking defects within micron-long oligopeptide stacks[32,63] could compromise the electronic delocalization over the full nanoaggregate, serving as a blockade to orbital overlap and even distribution of the electron density. However, as the NHOMO and HOMO have only a small energy difference of 0.02-0.03 eV at separations of d = 0.35-0.45 nm it is difficult to exploit this for charge-transfer excitations as its detection would require sharp energy resolution. Nevertheless, this observation renders this delocalization and the associated energy splitting a promising potential target for further engineering of this dimer. In addition, given uncertainties due to approximations in the computational framework used in this work, the small energy differences and balance between degeneracy and non-degeneracy of the NHOMO and HOMO also warrants further attention through simulations. We propose to test these hypotheses in follow-on work performing DFT calculations over multimeric stacks extracted from molecular dynamics simulations.

This combined classical mechanical/quantum mechanical investigation presents new understanding of the electronic origin of the relation between sequence, nanoaggregate morphology, and electronic properties. Specifically, DXX-OT4-XXD oligopeptides assemble into stacks with inter-peptide separations of $d \approx 0.45$ nm and twist angles that can be controlled over the range θ=0 – 25° by modulating the identity of the X residue. The dimer absorption spectrum is largely insensitive to twist angle over this range, but the degree of asymmetry in electron density sharing within the HOMO increases with θ. These results suggest that smaller X substitutions that produce more linear peptide stacks yield better electron delocalization over the self-assembled nanoaggregates and are more conducive to efficient charge transport. In addition to future calculations on multimeric stacks of peptides, we

also propose to extend this work to other peptide-π-peptide molecules to determine the generality of the observed sequence-structure-property relation and discern general design rules to engineer absorption spectra and electron delocalization.

Acknowledgments

This material is based upon work supported by the National Science Foundation under Grant No. DMR-1841807. This research is part of the Blue Waters sustained-petascale computing project, which is supported by the National Science Foundation (Grant Nos. OCI-0725070 and ACI-1238993) and the State of Illinois. Blue Waters is a joint effort of the University of Illinois at Urbana-Champaign and its National Center for Supercomputing Applications.

References

(1) Rad-Malekshahi, M.; Lempsink, L.; Amidi, M.; Hennink, W. E.; Mastrobattista, E. Biomedical applications of self-assembling peptides. *Bioconjugate Chem.* **2016**, *27*, 3–18.

(2) French, K. M.; Somasuntharam, I.; Davis, M. E. Self-assembling peptide-based delivery of therapeutics for myocardial infarction. *Advanced Drug Delivery Reviews* **2016**, *96*, 40–53.

(3) Dehsorkhi, A.; Castelletto, V.; Hamley, I. W. Self-assembling amphiphilic peptides. *J. Pept. Sci.* **2014**, *20*, 453–467.

(4) Hendricks, M. P.; Sato, K.; Palmer, L. C.; Stupp, S. I. Supramolecular assembly of peptide amphiphiles. *Acc. Chem. Res.* **2017**, *50*, 2440–2448.

(5) Caplan, M. R.; Lauffenburger, D. A. Nature's complex copolymers: Engineering design of oligopeptide materials. *Ind. Eng. Chem. Res.* **2001**, *41*, 403–412.

(6) Klok, H.-A.; Rosler, A.; Gotz, G.; Mena-Osteritz, E.; Bauerle, P. Synthesis of a silk-inspired peptide-oligothiophene conjugate. *Org. Biomol. Chem.* **2004**, *2*, 3541–3544.

(7) Diegelmann, S. R.; Gorham, J. M.; Tovar, J. D. One-dimensional optoelectronic nanostructures derived from the aqueous self-assembly of π-conjugated oligopeptides. *J. Am. Chem. Soc.* **2008**, *130*, 13840–13841.

(8) Mba, M.; Moretto, A.; Armelao, L.; Crisma, M.; Toniolo, C.; Maggini, M. Synthesis and self-assembly of oligo(p-phenylenevinylene) peptide conjugates in water. *Chemistry – A European Journal* **2011**, *17*, 2044–2047.

(9) Matmour, R.; De Cat, I.; George, S. J.; Adriaens, W.; Leclère, P.; Bomans, P. H. H.; Sommerdijk, N. A. J. M.; Gielen, J. C.; Christianen, P. C. M.; Heldens, J. T.; van Hest, J. C. M.; Löwik, D. W. P. M.; De Feyter, S.; Meijer, E. W.; Schenning, A. P.

H. J. Oligo(p-phenylenevinylene)-peptide conjugates: Synthesis and self-assembly in solution and at the solid-liquid interface. *J. Am. Chem. Soc.* **2008**, *130*, 14576–14583.

(10) Stone, D. A.; Hsu, L.; Stupp, S. I. Self-assembling quinquethiophene-oligopeptide hydrogelators. *Soft Matter* **2009**, *5*, 1990–1993.

(11) Zelzer, M.; Ulijn, R. V. Next-generation peptide nanomaterials: Molecular networks, interfaces and supramolecular functionality. *Chem. Soc. Rev.* **2010**, *39*, 3351–3357.

(12) Wall, B. D.; Zacca, A. E.; Sanders, A. M.; Wilson, W. L.; Ferguson, A. L.; Tovar, J. D. Supramolecular polymorphism: Tunable electronic interactions within π-conjugated peptide nanostructures dictated by primary amino acid sequence. *Langmuir* **2014**, *30*, 5946–5956.

(13) Kim, S. H.; Parquette, J. R. A model for the controlled assembly of semiconductor peptides. *Nanoscale* **2012**, *4*, 6940–6947.

(14) Hoeben, F. J. M.; Jonkheijm, P.; Meijer, E. W.; Schenning, A. P. H. J. About supramolecular assemblies of π-conjugated systems. *Chem. Rev.* **2005**, *105*, 1491–1546.

(15) Kale, T. S.; Marine, J. E.; Tovar, J. D. Self-assembly and associated photophysics of dendron-appended peptide-π-peptide triblock macromolecules. *Macromolecules* **2017**, *50*, 5315–5322.

(16) Sanders, A. M.; Magnanelli, T. J.; Bragg, A. E.; Tovar, J. D. Photoinduced electron transfer within supramolecular donor–acceptor peptide nanostructures under aqueous conditions. *J. Am. Chem. Soc.* **2016**, *138*, 3362–3370.

(17) Ardoña, H. A. M.; Tovar, J. D. Energy transfer within responsive pi-conjugated coassembled peptide-based nanostructures in aqueous environments. *Chem. Sci.* **2015**, *6*, 1474–1484.

(18) Mitschke, U.; Bauerle, P. The electroluminescence of organic materials. *J. Mater. Chem.* **2000**, *10*, 1471–1507.

(19) Roncali, J. Conjugated poly(thiophenes): Synthesis, functionalization, and applications. *Chem. Rev.* **1992**, *92*, 711–738.

(20) Fichou, D., Ed. *Handbook of Oligo- and Polythiophenes*; Wiley-VCH, 1999.

(21) Bian, L.; Zhu, E.; Tang, J.; Tang, W.; Zhang, F. Recent progress in the design of narrow bandgap conjugated polymers for high-efficiency organic solar cells. *Progress in Polymer Science* **2012**, *37*, 1292–1331.

(22) Guo, X.; Baumgarten, M.; Müllen, K. Designing π-conjugated polymers for organic electronics. *Prog. Polym. Sci.* **2013**, *38*, 1832–1908.

(23) Newman, C. R.; Frisbie, C. D.; da Silva Filho, D. A.; Brédas, J.-L.; Ewbank, P. C.; Mann, K. R. Introduction to organic thin film transistors and design of n-channel organic semiconductors. *Chem. Mater.* **2004**, *16*, 4436–4451.

(24) Hoppe, H.; Sariciftci, N. S. In *Photoresponsive Polymers II*; Marder, S. R., Lee, K.-S., Eds.; Springer Berlin Heidelberg: Berlin, Heidelberg, 2008; pp 1–86.

(25) Beaujuge, P. M.; Reynolds, J. R. Color control in π-conjugated organic polymers for use in electrochromic devices. *Chem. Rev.* **2010**, *110*, 268–320.

(26) Marty, R.; Szilluweit, R.; Sánchez-Ferrer, A.; Bolisetty, S.; Adamcik, J.; Mezzenga, R.; Spitzner, E.-C.; Feifer, M.; Steinmann, S. N.; Corminboeuf, C.; Frauenrath, H. Hierarchically structured microfibers of "single stack" perylene bisimide and quaterthiophene nanowires. *ACS Nano* **2013**, *7*, 8498–8508.

(27) White House Office of Science and Technology Policy, Materials Genome Initiative for Global Competitiveness. 2011.

(28) Ardoña, H. A. M.; Tovar, J. D. Peptide π-electron conjugates: Organic electronics for biology? *Bioconjugate Chem.* **2015**, *26*, 2290–2302.

(29) Ardoña, H. A. M.; Besar, K.; Togninalli, M.; Katz, H. E.; Tovar, J. D. Sequence-dependent mechanical, photophysical and electrical properties of pi-conjugated peptide hydrogelators. *J. Mater. Chem. C* **2015**, *3*, 6505–6514.

(30) Marciel, A. B.; Tanyeri, M.; Wall, B. D.; Tovar, J. D.; Schroeder, C. M.; Wilson, W. L. Fluidic-directed assembly of aligned oligopeptides with π-conjugated cores. *Adv. Mater.* **2013**, *25*, 6398–6404.

(31) Thurston, B. A.; Ferguson, A. L. Machine learning and molecular design of self-assembling -conjugated oligopeptides. *Molecular Simulation* **2018**, *44*, 930–945.

(32) Mansbach, R. A.; Ferguson, A. L. Control of the hierarchical assembly of π-conjugated optoelectronic peptides by pH and flow. *Org. Biomol. Chem.* **2017**, *15*, 5484–5502.

(33) Tovar, J. D. Supramolecular construction of optoelectronic biomaterials. *Acc. Chem. Res.* **2013**, *46*, 1527–1537.

(34) Sanders, A. M.; Kale, T. S.; Katz, H. E.; Tovar, J. D. Solid-phase synthesis of self-assembling multivalent π-conjugated peptides. *ACS Omega* **2017**, *2*, 409–419.

(35) Besar, K.; Ardoña, H. A. M.; Tovar, J. D.; Katz, H. E. Demonstration of hole transport and voltage equilibration in self-assembled π-conjugated peptide nanostructures using field-effect transistor architectures. *ACS Nano* **2015**, *9*, 12401–12409.

(36) Wall, B. D.; Zhou, Y.; Mei, S.; Ardoña, H. A. M.; Ferguson, A. L.; Tovar, J. D. Variation of formal hydrogen-bonding networks within electronically delocalized π-conjugated oligopeptide nanostructures. *Langmuir* **2014**, *30*, 11375–11385.

(37) Wall, B. D.; Diegelmann, S. R.; Zhang, S.; Dawidczyk, T. J.; Wilson, W. L.; Katz, H. E.; Mao, H.-Q.; Tovar, J. D. Aligned macroscopic domains of optoelectronic nanostructures

prepared via shear-flow assembly of peptide hydrogels. *Adv. Mater.* **2011**, *23*, 5009–5014.

(38) Valverde, L.; Thurston, B. A.; Ferguson, A. L.; Wilson, W. L. Evidence for prenucleated fibrilogenesis of acid-mediated self-assembling oligopeptides via molecular simulation and fluorescence correlation spectroscopy. *Langmuir* **2018**, *34*, 7346–7354.

(39) Thurston, B. A.; Tovar, J. D.; Ferguson, A. L. Thermodynamics, morphology, and kinetics of early-stage self-assembly of π-conjugated oligopeptides. *Molecular Simulation* **2016**, *42*, 955–975.

(40) Tsuzuki, S.; Honda, K.; Azumi, R. Model chemistry calculations of thiophene dimer interactions: Origin of π-stacking. *J. Am. Chem. Soc.* **2002**, *124*, 12200–12209.

(41) Scherlis, D. A.; Marzari, N. π-stacking in charged thiophene oligomers. *J. Phys. Chem. B* **2004**, *108*, 17791–17795.

(42) Luschtinetz, R.; Seifert, G. Theoretical studies on the structural and electronic properties of π-stacked cyano-thiophene-based molecules. *Comput. Theor. Chem.* **2013**, *1023*, 65 – 73.

(43) Liu, H.; Brémond, E.; Prlj, A.; Gonthier, J. F.; Corminboeuf, C. Adjusting the local arrangement of π-stacked oligothiophenes through hydrogen bonds: A viable route to promote charge transfer. *J. Phys. Chem. Lett.* **2014**, *5*, 2320–2324.

(44) Hotta, S.; Waragai, K. Alkyl-substituted oligothiophenes: Crystallographic and spectroscopic studies of neutral and doped forms. *J. Mater. Chem.* **1991**, *1*, 835–842.

(45) Siegrist, T.; Kloc, C.; Laudise, R. A.; Katz, H. E.; Haddon, R. C. Crystal growth, structure, and electronic band structure of α-4T polymorphs. *Adv. Mater.* **1998**, *10*, 379–382.

(46) DiCésare, N.; Belletête, M.; Garcia, E. R.; Leclerc, M.; Durocher, G. Intermolecular interactions in conjugated oligothiophenes. 3. Optical and photophysical properties of quaterthiophene and substituted quaterthiophenes in various environments. *J. Phys. Chem. A* **1999**, *103*, 3864–3875.

(47) Fabiano, E.; Sala, F. D.; Cingolani, R.; Weimer, M.; Görling, A. Theoretical study of singlet and triplet excitation energies in oligothiophenes. *J. Phys. Chem. A* **2005**, *109*, 3078–3085.

(48) Brédas, J. L.; Calbert, J. P.; da Silva Filho, D. A.; Cornil, J. Organic semiconductors: a theoretical characterization of the basic parameters governing charge transport. *Proc. Natl. Acad. Sci. U. S. A.* **2002**, *99*, 5804–5809.

(49) Macchi, G.; Medina, B. n. M.; Zambianchi, M.; Tubino, R.; Cornil, J.; Barbarella, G.; Gierschner, J.; Meinardi, F. Spectroscopic signatures for planar equilibrium geometries in methyl-substituted oligothiophenes. *Phys. Chem. Chem. Phys.* **2009**, *11*, 984–990.

(50) Tevis, I. D.; Palmer, L. C.; Herman, D. J.; Murray, I. P.; Stone, D. A.; Stupp, S. I. Self-assembly and orientation of hydrogen-bonded oligothiophene polymorphs at liquid-membrane-liquid interfaces. *J. Am. Chem. Soc.* **2011**, *133*, 16486–16494.

(51) Stone, D. A.; Tayi, A. S.; Goldberger, J. E.; Palmer, L. C.; Stupp, S. I. Self-assembly and conductivity of hydrogen-bonded oligothiophene nanofiber networks. *Chem. Commun.* **2011**, *47*, 5702–5704.

(52) Nicolaï, A.; Liu, H.; Petraglia, R.; Corminboeuf, C. Exploiting dispersion-driven aggregators as a route to new one-dimensional organic nanowires. *J. Phys. Chem. Lett.* **2015**, *6*, 4422–4428.

(53) Berendsen, H.; van der Spoel, D.; van Drunen, R. GROMACS: A message-passing parallel molecular dynamics implementation. *Chem. Phys. Commun.* **1995**, *91*, 43 – 56.

(54) Van Der Spoel, D.; Lindahl, E.; Hess, B.; Groenhof, G.; Mark, A. E.; Berendsen, H. J. C. GROMACS: Fast, flexible, and free. *J. Comput. Chem.* **2005**, *26*, 1701–1718.

(55) Wang, L.; Hingerty, B. E.; Srinivasan, A.; Olson, W. K.; Broyde, S. Accurate representation of B-DNA double helical structure with implicit solvent and counterions. *Biophys. J.* **2002**, *83*, 382–406.

(56) Hornak, V.; Abel, R.; Okur, A.; Strockbine, B.; Roitberg, A.; Simmerling, C. Comparison of multiple Amber force fields and development of improved protein backbone parameters. *Proteins: Structure, Function, and Bioinformatics* **2006**, *65*, 712–725.

(57) Reynolds, C. A.; Essex, J. W.; Richards, W. G. Atomic charges for variable molecular conformations. *J. Am. Chem. Soc.* **1992**, *114*, 9075–9079.

(58) Bayly, C. I.; Cieplak, P.; Cornell, W.; Kollman, P. A. A well-behaved electrostatic potential based method using charge restraints for deriving atomic charges: The RESP model. *J. Phys. Chem.* **1993**, *97*, 10269–10280.

(59) Vanquelef, E.; Simon, S.; Marquant, G.; Garcia, E.; Klimerak, G.; Delepine, J. C.; Cieplak, P.; Dupradeau, F.-Y. R.E.D. Server: a web service for deriving RESP and ESP charges and building force field libraries for new molecules and molecular fragments. *Nucleic Acids Research* **2011**, *39*, W511–W517.

(60) Frisch, M. J. et al. Gaussian 09. 2009.

(61) Wang, J.; Wang, W.; Kollman, P. A.; Case, D. A. Automatic atom type and bond type perception in molecular mechanical calculations. *J. Mol. Graph. Model.* **2006**, *25*, 247 – 260.

(62) Wang, J.; Wolf, R. M.; Caldwell, J. W.; Kollman, P. A.; Case, D. A. Development and testing of a general Amber force field. *J. Comput. Chem.* **2004**, *25*, 1157–1174.

(63) Mansbach, R. A.; Ferguson, A. L. Coarse-grained molecular simulation of the hierarchical self-assembly of π-conjugated optoelectronic peptides. *J. Phys. Chem. B* **2017**, *121*, 1684–1706.

(64) Jorgensen, W. L.; Chandrasekhar, J.; Madura, J. D.; Impey, R. W.; Klein, M. L. Comparison of simple potential functions for simulating liquid water. *J. Chem. Phys.* **1983**, *79*, 926–935.

(65) Essmann, U.; Perera, L.; Berkowitz, M. L.; Darden, T.; Lee, H.; Pedersen, L. G. A smooth particle mesh Ewald method. *J. Chem. Phys.* **1995**, *103*, 8577–8593.

(66) Hess, B.; Bekker, H.; Berendsen, H. J. C.; Fraaije, J. G. E. M. LINCS: A linear constraint solver for molecular simulations. *J. Comput. Chem.* **1997**, *18*, 1463–1472.

(67) Allen, M. P.; Tildesley, D. J. *Computer simulations of liquids*; Oxford University Press, 1989.

(68) Hockney, R.; Goel, S.; Eastwood, J. Quiet high-resolution computer models of a plasma. *J. Comput. Phys.* **1974**, *14*, 148–158.

(69) Bussi, G.; Donadio, D.; Parrinello, M. Canonical sampling through velocity rescaling. *J. Chem. Phys.* **2007**, *126*, 014101.

(70) Berendsen, H. J. C.; Postma, J. P. M.; van Gunsteren, W. F.; DiNola, A.; Haak, J. R. Molecular dynamics with coupling to an external bath. *J. Chem. Phys.* **1984**, *81*, 3684–3690.

(71) van der Spoel, D.; Lindahl, E.; Hess, B.; the GROMACS Development Team, GROMACS User Manual. Royal Institute of Technology and Uppsala Univerity, 2014.

(72) Nosé, S. A molecular dynamics method for simulations in the canonical ensemble. *Molecular Physics* **1984**, *52*, 255–268.

(73) Hoover, W. G. Canonical dynamics: Equilibrium phase-space distributions. *Phys. Rev. A* **1985**, *31*, 1695–1697.

(74) Nosé, S.; Klein, M. L. Constant pressure molecular dynamics for molecular systems. *Molecular Physics* **1983**, *50*, 1055–1076.

(75) Parrinello, M.; Rahman, A. Polymorphic transitions in single crystals: A new molecular dynamics method. *J. Appl. Phys.* **1981**, *52*, 7182–7190.

(76) Humphrey, W.; Dalke, A.; Schulten, K. VMD: Visual molecular dynamics. *Journal of Molecular Graphics* **1996**, *14*, 33–38.

(77) Chen, Z.; Stepanenko, V.; Dehm, V.; Prins, P.; Siebbeles, L. D.; Seibt, J.; Marquetand, P.; Engel, V.; Würthner, F. Photoluminescence and conductivity of self-assembled π–π stacks of perylene bisimide dyes. *Chemistry–A European Journal* **2007**, *13*, 436–449.

(78) Fink, R. F.; Seibt, J.; Engel, V.; Renz, M.; Kaupp, M.; Lochbrunner, S.; Zhao, H.-M.; Pfister, J.; Würthner, F.; Engels, B. Exciton trapping in π-conjugated materials: A quantum-chemistry-based protocol applied to perylene bisimide dye aggregates. *J. Am. Chem. Soc.* **2008**, *130*, 12858–12859.

(79) Klamt, A.; Schuurmann, G. COSMO: A new approach to dielectric screening in solvents with explicit expressions for the screening energy and its gradient. *J. Chem. Soc., Perkin Trans. 2* **1993**, 799–805.

(80) Miertuš, S.; Scrocco, E.; Tomasi, J. Electrostatic interaction of a solute with a continuum. A direct utilization of AB initio molecular potentials for the prevision of solvent effects. *Chem. Phys.* **1981**, *55*, 117 – 129.

(81) Kresse, G.; Furthmüller, J. Efficiency of ab-initio total energy calculations for metals and semiconductors using a plane-wave basis set. *Comp. Mater. Sci.* **1996**, *6*, 15–50.

(82) Kresse, G.; Joubert, D. From ultrasoft pseudopotentials to the projector augmented-wave method. *Phys. Rev. B* **1999**, *59*, 1758–1775.

(83) Blöchl, P. E. Projector augmented-wave method. *Phys. Rev. B* **1994**, *50*, 17953–17979.

(84) Perdew, J. P.; Wang, Y. Accurate and simple analytic representation of the electron-gas correlation energy. *Phys. Rev. B* **1992**, *45*, 13244–13249.

(85) Gajdoš, M.; Hummer, K.; Kresse, G.; Furthmüller, J.; Bechstedt, F. Linear optical properties in the projector-augmented wave methodology. *Phys. Rev. B* **2006**, *73*, 045112.

(86) Blaiszik, B.; Chard, K.; Pruyne, J.; Ananthakrishnan, R.; Tuecke, S.; Foster, I. The Materials Data Facility: Data services to advance materials science research. *JOM* **2016**, *68*, 2045–2052.

(87) Thurston, B.; Shapera, E.; Tovar, J.; Schleife, A.; Ferguson, A. Self-assembled peptide absorption spectra. *Materials Data Facility* **2019**, doi: 10.18126/T28A–UWGW.

(88) Blaiszik, B.; Ward, L.; Schwarting, M.; Gaff, J.; Chard, R.; Pike, D.; Chard, K.; Foster, I. A data ecosystem to support machine learning in materials science. *arXiv preprint* **2019**, *arXiv:1904.10423*.

(89) Kuo, S.-W. *Hydrogen bonding in polymeric materials*; John Wiley & Sons, 2018.

(90) Petsko, G. A.; Ringe, D. *Protein structure and function*; New Science Press, 2004.

(91) Birkbeck College (University of London), 1995; `http://www.cryst.bbk.ac.uk/PPS95/course/3_geometry/sheet.html`.

TOC Graphic